

A Ubiquitous Unifying Degeneracy in 2-body Microlensing Systems

Keming Zhang, B. Scott Gaudi, Joshua S. Bloom

2021-11-30

Abstract

While gravitational microlensing by planetary systems [3, 4] can provide unique vistas on the properties of exoplanets [5], observations of such 2-body microlensing events can often be explained with multiple and distinct physical configurations, so-called model degeneracies. An understanding of the intrinsic and exogenous origins of different classes of degeneracy provides a foundation for phenomenological interpretation. Here, leveraging a fast machine-learning based inference framework [6], we present the discovery of a new regime of degeneracy—the *offset* degeneracy—which unifies the previously known *close-wide* [7, 8] and *inner-outer* [9] degeneracies, generalises to resonant caustics, and upon reanalysis, is ubiquitous in previously published planetary events with 2-fold degenerate solutions. Importantly, our discovery suggests that the commonly reported *close-wide* degeneracy essentially never arises in actual events and should, instead, be more suitably viewed as a transition point of the *offset* degeneracy. While previous studies of microlensing degeneracies are largely studies of degenerate *caustics*, our discovery demonstrates that degenerate *caustics* do not necessarily result in degenerate *events*, which for the latter it is more relevant to study magnifications *at* the location of the source. This discovery fundamentally changes the way in which degeneracies in planetary microlensing events should be interpreted, suggests a deeper symmetry in the mathematics of 2-body lenses than has previously been recognised, and will increasingly manifest itself in data from new generations of microlensing surveys.

Microlensing appears as the time-varying magnification and astrometric deflection of a background star when a foreground system of stellar objects passes close to the line of sight of the background star. If the foreground system contains more than one body, the resultant complex light curve can be analysed to infer some properties of the lens system, in particular the mass ratios q and projected separations s between the individual bodies [5] in units of the angular Einstein radius¹ (θ_E), which is the characteristic scale for gravitational lensing. To date, >100 exoplanets have been discovered with microlensing² with thousands more expected as

¹Here, $\theta_E = \sqrt{\kappa M \pi_{rel}}$, where $\kappa = 4G/(c^2 \text{AU})$, M is the total lens mass, and $\pi_{rel} = \text{AU}/D_{rel}$ is the lens-source relative parallax. See [5]

²<https://exoplanetarchive.ipac.caltech.edu>. Accessed 08/21/2021.

next-generation microlensing surveys further extend the sensitivity limit from space [10, 11].

For a given 2-body lens configuration, the expected time-varying magnification signal can be accurately predicted [12] using General Relativity [13] with the gravitational lens equation [14]. However, a given set of observations is not guaranteed to map back to a unique lens configuration: there are often multiple, distinct sets of parameters that adequately explain the data. Facing such a potentially ambiguous solution space, it is vital to have prior knowledge and understanding of possible degeneracies to ensure that all viable solutions are properly recovered in the analysis of individual events.

While some degeneracies arise due to insufficient time coverage or low data quality, there exists so-called “mathematical” degeneracies that arise from symmetries of the gravitational lens equation itself that appear in certain limits, and therefore persist even in the presence of the highest quality of data. Those degeneracies are best understood by considering microlensing caustics, which are the loci of points where a point source would formally be infinitely magnified by the foreground lens, and can be classified into three regimes for 2-body lenses: close, resonant, and wide [14] (Extended Data Figure 1). As significant deviations from the single-lens magnification occur near caustics, an understanding of caustic properties has been considered to provide insight into the phenomenology, and thus degeneracies, of two-body microlensing events.

There are two well-studied mathematical degeneracies: the *close-wide* degeneracy [7, 8] and the *inner-outer* degeneracy [9], which applies to sources passing close to the central or planetary caustics, respectively. For the *close-wide* degeneracy, the central caustic shape is known to be invariant under the $s \leftrightarrow s^{-1}$ transformation for $|1 - s| \gg q^{1/3}$ and $q \ll 1$ [21] (Extended Data Figure 1a,c). This invariance has been cited to explain degeneracies in planetary events where the source passes close to the primary star, and thus the central caustic. For the *inner-outer* degeneracy, the planetary caustic(s) in the same condition of $|1 - s| \gg q^{1/3}$ and $q \ll 1$ is well approximated by a Chang-Refsdal lens that is symmetrical along the star-planet axis [2]. Therefore, sources passing either side of the planetary caustic are expected to create similar magnification patterns (Figure 1a,i; Extended Data Figure 2d,h). In both cases, q is expected to be similar for the two degenerate solutions, but in the *close-wide* case, there is ambiguity as to whether the planet is close-in (e.g., separations similar to Earth or Mars), or far-out (e.g., separations similar to Jupiter or Saturn), thus affecting studies of statistical properties of exoplanets.

To probe the existence of new degeneracies, we examined the posterior parameter distributions of a large number simulated binary-lens, single-source (2L1S) events that exhibited multi-modal solutions. While such an endeavour would generally be computational prohibitive with the current *status-quo* microlensing data analysis approaches, our effort has been made possible by the recent application of likelihood-free-inference (LFI) [15] to 2-body microlensing [6]. The key to the LFI approach is the *Neural Density Estimator* (NDE), which is a particular type of neural network capable of learning conditional distributions that are complex and multi-modal. Observing that the posterior is a conditional distribution, we trained a NDE on 691,257 events simulated in the context of the next generation *Roman Space Telescope* microlensing survey [11]. The trained NDE can then infer posterior parameter distributions for any future event unseen during training within seconds, effectively in real time. To isolate events with multi-modal solutions, we apply a clustering algorithm [16] which classifies each of the posteriors into discrete clusters/modes (see Methods). This approach effectively allowed us to “preview” the degeneracies that would be encountered with the increased sensitivity of *Roman*.

Visual inspection of NDE-derived, multi-modal posteriors for planetary events reveals three apparent regimes of degeneracy: the *inner-outer* degeneracy, the *close-wide* degeneracy, and degeneracies that involve the resonant caustic which have been observed (e.g. [1, 49]) and stud-

ied before [20, 21]. Interestingly, we found that most cases of apparent *close-wide* degeneracies do not exactly abide by the $s \leftrightarrow 1/s$ relation even though most are in the regime where this degeneracy is expected to hold, namely $|1 - s| \gg q^{1/3}$ and $q \ll 1$ [21]. We also note that for degenerate events involving one resonant caustic, the source trajectory always passes to the front end of the caustic for *wide-resonant* degenerate events, and the back end for *close-resonant* degenerate events.

To explore potential connections among these apparently discrete regimes of degeneracies, and to better understand the reason why the expected $s \leftrightarrow 1/s$ relation of the *close-wide* degeneracy is almost never satisfied, we examined maps of magnification differences between pairs of lenses with the same mass-ratio ($q = 2 \times 10^{-4}$), keeping lens B fixed at $s_B = 1/1.1$ and changing the projected separation s_A of lens A. The sequence of magnification difference maps immediately reveals the existence and continuous evolution of an oval-shaped ring where the magnification difference between the lens A/B vanishes (Fig. 1a–h; also see Extended Data Figure 2 for $s_B = 1.18$). This *null* ring originates near the centre of the central/resonant caustic and intersects the star-planet axis at increasing distances with increasing deviation from the *close-wide* degenerate configuration of $s_A = 1/s_B$, at which point the *null* contracts to a point (see Extended Figure 5 for a zoom-in). This suggests the existence of trajectory dependent, localised degeneracies, which is further confirmed by the 1D magnification slices (light curves) in Fig. 1i–h that shows the exact magnification matching of null-passing trajectories (cyan arrows in Fig. 1a–h).

Furthermore, the most surprising revelation is that none of those trajectories, including caustic crossing trajectories (Fig. 1n), result in degenerate light curves under the *close-wide* degenerate configuration of $s_A = 1/s_B$. The implication is both profound and surprising: the $s \leftrightarrow 1/s$ duality of the *close-wide* degeneracy should essentially never be expected to manifest in actual events. As a first step exploring this surprising conclusion, we first examined the null structure dependence on q . Extended Data Fig. 3 shows that the *null* location on the star-planet axis is independent of q for $q \ll 1$. Thus, for any given pair of $s_{A,B}$, the mass-ratio can be lowered arbitrarily to satisfy the formal $|1 - s| \gg q^{1/3}$ condition where the *close-wide* degeneracy is expected to hold, but still maintain the null structure. This demonstrates that the above localised degeneracy does not arise due to the imperfect matching of the shape of the central caustic, but is an fundamental behaviour of the lensing system.

We name this new phenomenon the *offset* degeneracy, because, as opposed to the previous notion of a *static close-wide* degeneracy that is independent of the source trajectory, it is now understood that the projected separations ($s_{A,B}$) of the degenerate lens configurations should always be offset from the *static* $s_A = 1/s_B$ solution such that the location of the *null* on the star-planet axis coincides with the source trajectory. Notably, we found that the location of the *null* on the star-planet axis is well described by a simple expression:

$$x_{\text{null}} = \frac{1}{2} (s_A - 1/s_A + s_B - 1/s_B), \quad (1)$$

Numerically determined x_{null} (Extended Data Figure 2) shows that deviations from this analytic prescription is consistently less than 5% except for extreme separation ($|\log_{10}(s_{A,B})| \gtrsim 0.5$), opposite topology cases that generally do not yield significant planetary perturbations³. This expression can be interpreted as the midpoint between the locations $x_c = s_{A,B} - 1/s_{A,B}$ of the planetary caustics, which arises from the perturbative picture of planetary microlensing [4].

³since the trajectory is constrained by the location of the null, which is far from either central or planetary caustics

However, the fact that the such an expression holds well into the resonant regime for which there are no planetary caustics at all, and persists through caustic topology changes, likely suggests much deeper symmetries in gravitational lens equation for mass ratios of $q \ll 1$ than had previously been appreciated.

We suggest that the connection of Equation 1 to the two previously known mathematical degeneracies has deep implications. By setting $x_{null} = 0$ in Equation 1, one immediately recovers the $s_A = 1/s_B$ relation. This further corroborates our finding that the *close-wide* degeneracy is never strictly realised in actual events except for the singular case⁴ of $u_0 = 0$. Thus, we now see that the *close-wide* degeneracy should be more suitably viewed as a transition point of the *offset* degeneracy where the central caustics *happen* to be degenerate. Furthermore, an expression similar to Equation 1 has also been noted for the *inner-outer* degeneracy [9] which arises due to the symmetry of the Chang-Refsdal caustic approximation. Strictly speaking, however, this symmetry cannot exactly account for such degeneracies seen in actual events, both because most observed *inner-outer* degeneracies are not in the Chang-Refsdal regime, and because even for well-separated planetary caustics in the Chang-Refsdal limit, the two degenerate caustics are different (i.e. have different values of s). The above dilemma is relieved by considering the empirical *inner-outer* degeneracy as one regime of the *offset* degeneracy, which does not reference particular caustics. Therefore, the *offset* degeneracy not only unify the two previously known degeneracies into a generalised regime, but also relaxes the $|1-s| \gg q^{1/3}$ condition required by both cases.

Based on the arguments above, we expected the *offset* degeneracy to be ubiquitous in past events with degenerate solutions and speculate that a large number of cases may have been mistakenly attributed to the *close-wide* degeneracy. Therefore, we systematically searched for previously-published events with two-fold degenerate solutions satisfying $q_A \simeq q_B \ll 1$ (see Methods). We found 25 such events, and then first compared the intersection of the source trajectory on the star-planet axis to the location of the *null* predicted with Equations 1. We also invert Equation 1 to predict the degenerate s_A from a known solution s_B :

$$s_A = \frac{1}{2} \left(2x_0 - (s_B - 1/s_B) + \sqrt{[2x_0 - (s_B - 1/s_B)]^2 + 4} \right), \quad (2)$$

where $x_0 = u_0/\sin(\alpha)$ is the intercept of the source trajectory on the binary axis, u_0 is the impact parameter, and α is the angle of the source trajectory with respect to the binary axis. As shown in Figure 3, the source trajectory always passes through the *null* location on the star-planet axis as predicted by Equation 1. Additionally, Equation 2 accurately predicts one degenerate solution from the other. The fact that Equation 2 applies for a wide range of α confirms that the *offset* degeneracy accommodates oblique trajectories, although proximity to planetary caustics might break the degeneracy (e.g., KMT-2016-BLG-1397 [17]). Thus we conclude that Equation 2 will be useful in the analysis of future events with *offset*-degenerate solutions.

Given its apparent ubiquity, it is reasonable to ask why the *offset* degeneracy has only been discovered over two decades after the first in-depth explorations of degeneracies in two-body microlensing events [2, 7, 8]. On the conceptual side, previous studies of microlensing degeneracies have largely been focused on invariances and symmetries of caustics in isolation. However, our work has showed that *caustic* degeneracies do not necessarily, and in the case of the *close-wide* degeneracy, never result in *event* degeneracies. In case of degeneracies in actual

⁴In this case u_0 is defined with respect to the null convergence point near the caustic centre (see Extended Figure 5).

events, it may be more instructive to directly study the magnification-matching behaviour at the location of the source.

Another reason may be the early strategic focus on high-magnification ($u \ll 1$) events [7, 19], where deviations from $s \leftrightarrow s^{-1}$ were small and whose cause was not explored in detail. Recently, such deviations have become increasingly manifest in mid-magnification and semi-resonant events which has led to some explicit discussions. Facing a degenerate event in the resonant regime (OGLE-2019-BLG-0960) where the two solutions deviated from the $s \leftrightarrow s^{-1}$ relation, [20] suggested a “‘close’-‘wide’ degeneracy for semi-resonant caustics”, where the *close-wide* degeneracy merged with the *inner-outer* degeneracy for $s \rightarrow 1$. The theoretical follow-up work of [21] further clarified the exact conditions of the *close-wide* degeneracy and its applicability to the resonant regime. Nevertheless, as we have shown, the resonant condition does not cause the deviation from $s \leftrightarrow s^{-1}$, but only allows it to be noticeable (see Methods). To our advantage, the novel ML-based technique of [6] presented us with a large number of degenerate events in non-resonant $|1 - s| \gg q^{1/3}$ regime that deviated from the $s \leftrightarrow s^{-1}$ expectation, but also did not conform to the *inner-outer* degeneracy. These ‘intermediate’ *offset*-degenerate events ultimately allowed us to recognise the continuous and unifying nature of the *offset* degeneracy.

We close by suggesting that current discovery represents a new milestone for the growing utility of machine learning in the physical sciences. To date, machine learning has been widely applied to astronomical data analysis pipelines for regression and classification tasks, acting as accelerants to discovery of natural phenomenology. To our knowledge, however, the discovery of the *offset* degeneracy is the first example where ML directly yields new mathematical insight in astrophysics. The approach presented in this paper may also be fruitfully applied to studies of degeneracies in other fields with computationally expensive inference conditions.

References

- [1] Herrera-Martin, A. *et al.* OGLE-2018-BLG-0677Lb: A Super-Earth Near the Galactic Bulge. *The Astronomical Journal* **159**, 256 (2020). URL <https://iopscience.iop.org/article/10.3847/1538-3881/ab893e>.
- [2] Gaudi, B. S. & Gould, A. Planet Parameters in Microlensing Events. *The Astrophysical Journal* **486**, 85 (1997). URL <https://iopscience.iop.org/article/10.1086/304491/meta>. Publisher: IOP Publishing.
- [3] Mao, S. & Paczyński, B. Gravitational Microlensing by Double Stars and Planetary Systems. *ApJ* **374**, L37 (1991).
- [4] Gould, A. & Loeb, A. Discovering planetary systems through gravitational microlenses. *The Astrophysical Journal* **396**, 104–114 (1992). URL <http://adsabs.harvard.edu/abs/1992ApJ...396..104G>.
- [5] Gaudi, B. S. Microlensing Surveys for Exoplanets. *Annual Review of Astronomy and Astrophysics* **50**, 411–453 (2012). URL <http://www.annualreviews.org/doi/10.1146/annurev-astro-081811-125518>.
- [6] Zhang, K. *et al.* Real-time Likelihood-free Inference of Roman Binary Microlensing Events with Amortized Neural Posterior Estimation. *The Astronomical Journal* **161**,

- 262 (2021). URL <https://doi.org/10.3847/1538-3881/abf42e>. Publisher: American Astronomical Society.
- [7] Griest, K. & Safizadeh, N. The Use of High-Magnification Microlensing Events in Discovering Extrasolar Planets. *The Astrophysical Journal* **500**, 37 (1998). URL <https://iopscience.iop.org/article/10.1086/305729/meta>. Publisher: IOP Publishing.
 - [8] Dominik, M. The binary gravitational lens and its extreme cases. *A&A* **349**, 108–125 (1999). [astro-ph/9903014](https://arxiv.org/abs/astro-ph/9903014).
 - [9] Han, C. *et al.* MOA-2016-BLG-319Lb: Microlensing Planet Subject to Rare Minor-image Perturbation Degeneracy in Determining Planet Parameters. *The Astronomical Journal* **156**, 226 (2018). URL <https://doi.org/10.3847/1538-3881/aae38e>. Publisher: American Astronomical Society.
 - [10] Bennett, D. P. & Rhie, S. H. Simulation of a Space-based Microlensing Survey for Terrestrial Extrasolar Planets. *The Astrophysical Journal* **574**, 985 (2002). URL <https://iopscience.iop.org/article/10.1086/340977/meta>. Publisher: IOP Publishing.
 - [11] Penny, M. T. *et al.* Predictions of the WFIRST Microlensing Survey I: Bound Planet Detection Rates. *The Astrophysical Journal Supplement Series* **241**, 3 (2019). URL <http://arxiv.org/abs/1808.02490>. ArXiv: 1808.02490.
 - [12] Poleski, R. & Yee, J. C. Modeling microlensing events with MulensModel. *Astronomy and Computing* **26**, 35 (2019). [1803.01003](https://arxiv.org/abs/1803.01003).
 - [13] Einstein, A. Lens-Like Action of a Star by the Deviation of Light in the Gravitational Field. *Science* **84**, 506–507 (1936).
 - [14] Schneider, P. & Weiss, A. The two-point-mass lens - Detailed investigation of a special asymmetric gravitational lens. *A&A* **164**, 237–259 (1986).
 - [15] Cranmer, K., Brehmer, J. & Louppe, G. The frontier of simulation-based inference. *Proceedings of the National Academy of Sciences* **117**, 30055–30062 (2020). URL <https://www.pnas.org/content/117/48/30055>. <https://www.pnas.org/content/117/48/30055.full.pdf>.
 - [16] Campello, R. J. G. B., Moulavi, D. & Sander, J. Density-Based Clustering Based on Hierarchical Density Estimates. In Pei, J., Tseng, V. S., Cao, L., Motoda, H. & Xu, G. (eds.) *Advances in Knowledge Discovery and Data Mining*, Lecture Notes in Computer Science, 160–172 (Springer, Berlin, Heidelberg, 2013).
 - [17] Zang, W. *et al.* KMT-2016-BLG-1397b: KMTNET-only discovery of a microlens giant planet. *The Astronomical Journal* **156**, 236 (2018). URL <https://doi.org/10.3847/1538-3881/aae537>.
 - [18] Bond, I. A. *et al.* OGLE 2003-BLG-235/MOA 2003-BLG-53: A planetary microlensing event. *The Astrophysical Journal* **606**, L155–L158 (2004). URL <https://doi.org/10.1086/420928>.

- [19] Gould, A. *et al.* Frequency of Solar-like Systems and of Ice and Gas Giants Beyond the Snow Line from High-magnification Microlensing Events in 2005-2008. *ApJ* **720**, 1073–1089 (2010). [1001.0572](#).
- [20] Yee, J. C. *et al.* OGLE-2019-BLG-0960Lb: The Smallest Microlensing Planet. *arXiv:2101.04696 [astro-ph]* (2021). URL <http://arxiv.org/abs/2101.04696>. ArXiv: 2101.04696.
- [21] An, J. On the condition for the central caustic degeneracy of the planetary microlensing. *arXiv:2102.07950 [astro-ph]* (2021). URL <http://arxiv.org/abs/2102.07950>. ArXiv: 2102.07950.
- [22] Petters, A. O., Levine, H. & Wambsganss, J. *Singularity theory and gravitational lensing* (2001).

Acknowledgements

K.Z. thanks the LSSTC Data Science Fellowship Program, which is funded by LSSTC, NSF Cybertraining Grant #1829740, the Brinson Foundation, and the Moore Foundation; his participation in the program has benefited this work. K.Z. and J.S.B are supported by a Gordon and Betty Moore Foundation Data-Driven Discovery grant. Work by B.S.G. is supported by NASA grant NNG16PJ32C and the Thomas Jefferson Chair for Discovery and Space Exploration. We thank Eric Agol and Jessica Lu for helpful comments on a draft of this manuscript.

Author information

Contributions

K.Z. and J.S.B. conceived of the degeneracy-finding search. K.Z. implemented the search and identified the offset degeneracy. J.S.B. designed and wrote the code for the cluster-finding approach. B.S.G. aided in the study and interpretation of the LFI-derived posteriors of microlensing events, helped to develop the interpretation of the offset degeneracy and place it in the context of results from the literature. K.Z., B.S.G., and J.S.B. co-wrote the manuscript.

Affiliations

Department of Astronomy, University of California, Berkeley, CA 94720, USA.

K. Zhang, J. S. Bloom

Department of Astronomy, The Ohio State University, Columbus, OH 43210, USA.

B. S. Gaudi

Corresponding author

Correspondence to K. Zhang.

Methods

The Z21 fast inference technique

Zhang et al. [6] (Z21 hereafter) presented a LFI-based method for binary microlensing inference that allows the posterior for any given event to be computed automatically in seconds. We summarise the Z21 approach at the high level here, and refer the reader to their original paper for details.

The Z21 method is likelihood-free in that it does not iteratively perform simulations to compute the likelihood (goodness-of-fit), which is typical for sampling-based inference methods. Instead, Z21 directly learns the posterior probability as a conditional distribution $\hat{p}_\phi(\theta|x)$ with a neural network (NN), where ϕ are the NN parameters, θ the 2LIS parameters, and x the input light curve. The model takes an input light curve and produces a specified number of discrete posterior samples. The NN learns such a distribution from a training set of a large number of

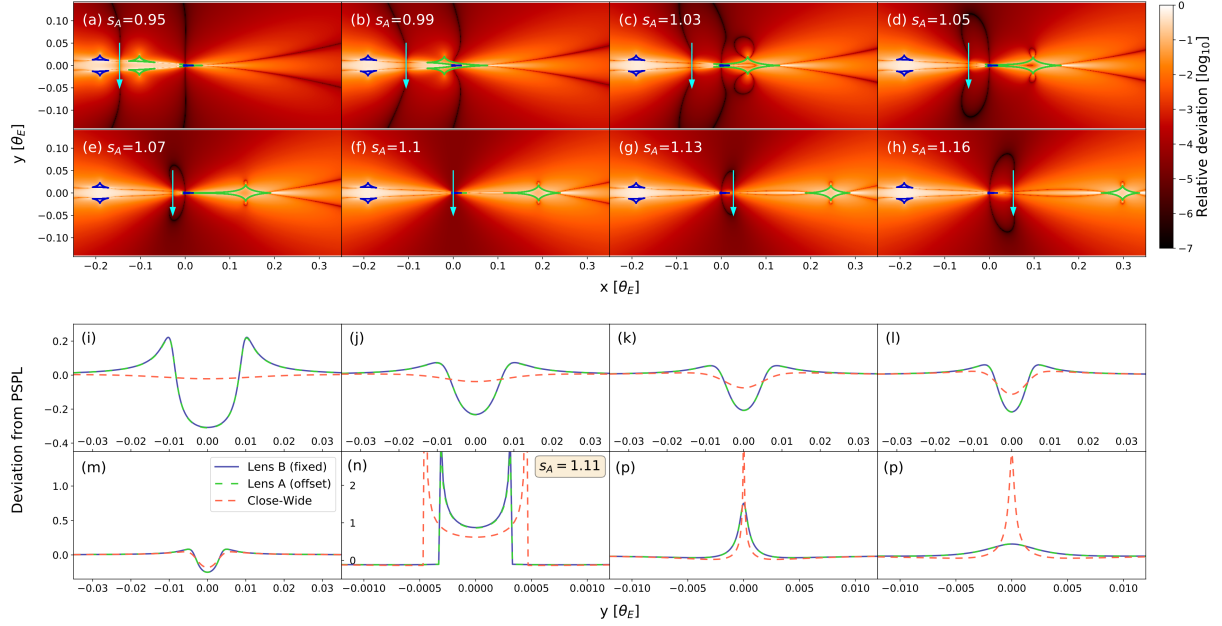


Figure 1: The manifestation of the *offset* degeneracy in the source-plane magnification differences maps (top) and light curve differences (bottom). (a)–(h): Maps of magnification differences from lens B with fixed $s_B = 1/1.1$ to lens A with changing s_A specified in each subplot. All magnification difference maps are shown on the same scale, specified in the color-bar to the right. Lens A caustics are shown in green and lens B caustics are shown in blue. The black, oval-shaped ring with first decreasing and then increasing sizes in (a)–(h) is the null where the magnification difference between lens A/B vanishes. The evolution of the null ring is continuous with the progression of the lens A caustic into the resonant regime (e, f, g) and further into a close topology (h). (i)–(p): Light curves for the vertical trajectories passing through the *null* indicated with cyan arrows in (a)–(h), for lens A (blue), lens B (green), and the $s_A = 1/s_B = 1.1$ solution (red) expected from the close-wide degeneracy. Light curves are shown as relative deviations from the corresponding point-source point-lens (PSPL) model. Subplot (n) is shown for $s_A = 1.11$ instead to demonstrate the *offset* degeneracy for caustic crossing events: both caustic-crossing length and magnification patterns are matched for the *offset* solution but not for the *close-wide* solution.

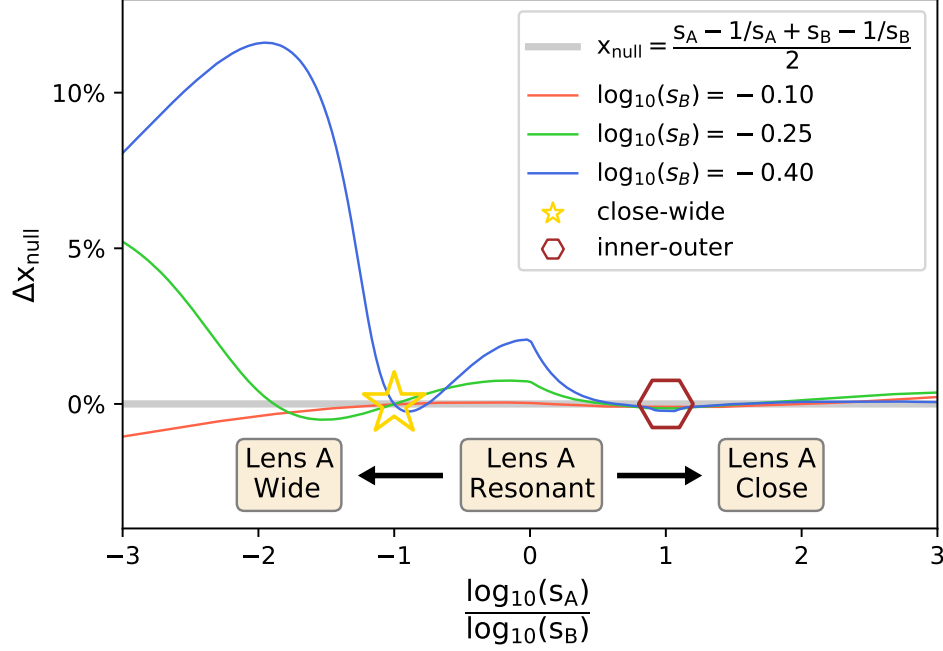


Figure 2: Deviation (Δx_{null}) of numerically-derived null position from the analytic form (Equation 1) for changing s_A against three values of fixed $s_B < 1$, normalised to the separation between the two (implied) planetary caustics: $|(s_A - 1/s_A) - (s_B - 1/s_B)|$. Δx_{null} is calculated for $q = 2 \times 10^{-4}$ but was found to be independent of q for $q \ll 1$ (Extended Figure 3). The x-axis shows $\log_{10}(s_A)$ scaled to $\log_{10}(s_B)$ such that -1 corresponds to the *close-wide* case of $s_A = 1/s_B$ (gold star), 0 corresponds to exact resonance for lens A ($s_A = 1$), and 1 corresponds to the asymptotic *inner-outer* case where $s_A = s_B$ (brown hexagon). The same curves for $\log_{10}(s_B) = 0.1, 0.25, 0.4$ can be found by inverting the y-axis: $\Delta x_{\text{null}}(-\log_{10}(s_B)) = -\Delta x_{\text{null}}(\log_{10}(s_B))$.

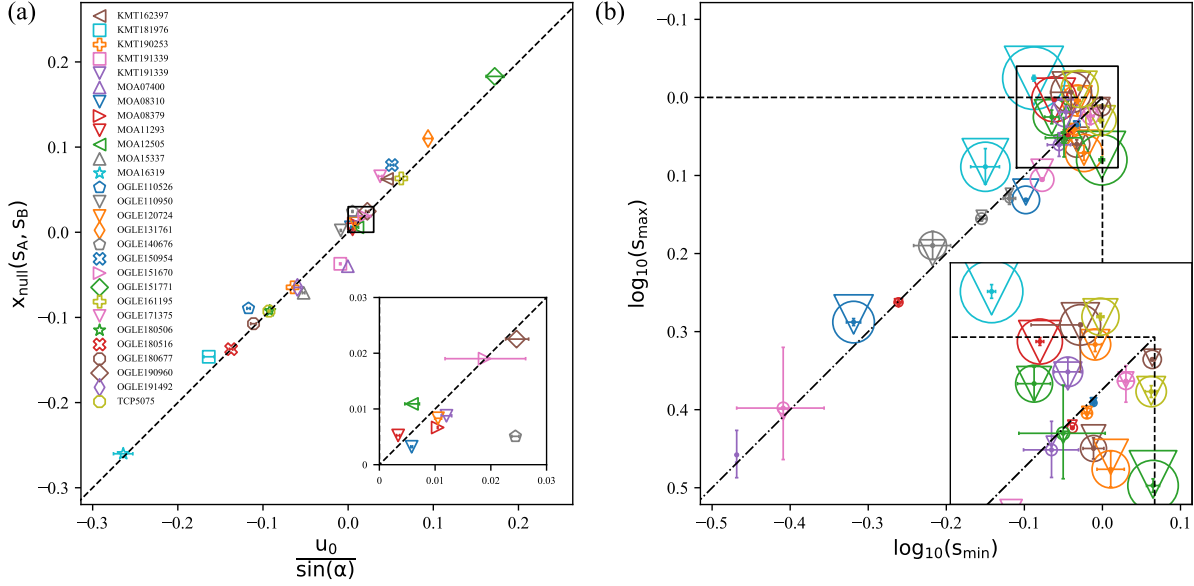


Figure 3: *Offset* degeneracy reanalysis of 25 systematically selected events in the literature with two-fold degenerate solutions. (a) confirms that the source trajectory always close to the null intersection on the star-planet axis (x_{null}) as predicted by Equation 1. The horizontal axis shows the source trajectory intercept on the binary axis, calculated from the impact parameter (u_0) and trajectory angle (α). The vertical axis shows the prediction for x_{null} using Equation 1 and reported values of s_A and s_B . Event labels as shown in the legend are the event abbreviations: for example, KMT162397 means KMT-2016-BLG-2397. The inset shows zoom-in of the central boxed region. (b) The x and y-axis show the smaller and larger value of the degenerate $s_{A,B}$ solutions. Circles are reported values of $s_{\min, \max}$ whereas triangles are s_{\max} values predicted with Equation 2 of the *offset* degeneracy and s_{\min} , α , and u_0 . Circles and triangles largely coincide for all cases, demonstrating the predictive power of the *offset* degeneracy. The same colour coding follows from the legend in (a). The dash-dotted line represent the exact *close-wide* degeneracy where $s_{\min} = 1/s_{\max}$. Cases typically understood as *inner-outer* — $s_{A,B} > 1$ or $s_{A,B} < 1$ — are found outside the box bounded by the dashed lines. Cases close to the dashed lines but far their conjunction correspond to *resonant-close/wide* degeneracies. Cases within the dashed box and not on the diagonal line do not belong to either *close-wide* or *inner-outer* degeneracies. The inset shows zoom-in of the region boxed by solid lines. Error-bars are marginalised 1- σ posterior intervals.

simulations (x_i, θ_i) , where the NN parameters (ϕ) are optimised to maximise the expectation of that conditional probability under the training set data distribution. The distribution learned is therefore a global posterior without reference to particular event, such that it can be applied to any future events unseen during training.

This specific approach to LFI is called *amortised neural posterior estimation*, where “amortised” refers to the process of paying all simulation cost upfront so that inferences of future events do not require additional simulations. After training, the NN alone generates posterior samples for any future event at a rate of $\sim 10^6 \text{ s}^{-1}$ on a consumer grade GPU, or $\sim 10^5 \text{ s}^{-1}$ on a 8-core CPU, effectively doing inference in real time. Z21 demonstrated that, although not exact, the neural posterior places meaningful constraints on all parameters nearly 100% of the time, except for the parameter that quantifies the effect of a finite-sized source. This is because

For our results to have direct implications to the next generation, space-based [10] microlensing survey planned on the *Roman Space Telescope* [11], we generated a training set in a similar fashion as the Z21 training set, but with a caustic-centred coordinate system rather than a centre-of-mass (COM) coordinate system. This is because the COM coordinate system is highly inefficient for producing planetary-caustic passing events with randomly drawn source trajectories with respect to the COM. In addition, for wide binary ($s > 1$; $q \sim 1$) events, the time-to-closest-approach (t_0) to the COM could be have an arbitrarily large offset from the time of peak magnification, which could cause missing degenerate modes (see Section 4.3 of Z21). The caustic-centred coordinate system, on the other hand, efficiently spans the entire 2L1S parameter space which allows for significant deviation from a single-lens light curve.

We generate a total of 228,892 events centred on the planetary caustic and 960,000 events centred on the central caustic, and further remove those that are consistent with a single lens model. This results in a training set of 691,257 simulations, including 137,644 planetary caustic events and 553,863 central caustic events.

For planetary caustic events, u_0 are randomly sampled from 0 to 50 times the caustic size. For central caustic events, u_0 are randomly sampled from 0 to 2. Compared to Z21, we expanded

the source flux fraction, defined as $f_s = \frac{F_{\text{source}}}{F_{\text{source}} + F_{\text{blend}}}$, to $f_s \sim \text{LogUniform}(0.05, 1)$, to probe deeper into the severely blended regime. Other aspects of event simulation are the same with Z21 and the reader is referred to Section 3 of Z21 for details.

Identifying degeneracies in Z21 posteriors

Z21 provided three example events with degenerate posteriors where light curve realisations from each degenerate mode are almost indistinguishable from one another, a confirmation of its efficacy in modelling data with degenerate solutions. While the posterior modes in Z21 were identified manually, here we would like to automate the degeneracy-finding process.

To work with posterior distributions that vary in scale, position, and shape, we first fit and apply a parametric, monotonic “power” transformation [23] to the LFI-generated posterior samples for each simulated light curve. This transformation normalises each marginal parameter distribution to an approximate Gaussian. To automatically identify degenerate posteriors, we use the HDBSCAN algorithm [16] to perform clustering on the transformed posterior samples. The HDBSCAN algorithm is a density-based, hierarchical clustering method which required, for our task, little hyperparameter tuning. The output of HDBSCAN is a suggested cluster label for each posterior sample, including the labelling for outlier/noise samples. Events with more than one cluster are identified as degenerate events.

Although the Z21 posteriors are accurate enough for a qualitative study of degeneracies, we

nevertheless refine each solution mode to the best-fit value. The known distribution for each posterior mode allows us to make use of bounded optimisation algorithms to quickly locate the exact solution. We use a parallel implementation [24] of the L-BFGS-B optimisation algorithm [25] to quickly solve for the best fit solutions. The entire process from light curve to degenerate exact solutions takes a few minutes for each event, with the last refinement step costing the most time.

Comparison to events in the literature

We demonstrated the ubiquitous existence of the offset degeneracy by attempting a thorough investigation into published 2L1S events in the literature with reported degenerate posteriors. We first filter through events on the NASA microlensing exoplanet archive⁵ which contains 112 planets and 306 entries with reported 2L1S parameters. Each entry reports one solution for a given event.

Entries from adaptive-optics follow-up papers of published events, as well as duplicate entries with identical 2L1S solutions are first removed. Triple lens events with detections of two planets — OGLE-2006-BLG-109 and OGLE-2018-BLG-1011 — are also removed. Planets with reported higher-order effects (parallax, xallarap) are also removed, as such effects often exhibit additional degeneracies and may complicate the application of the offset degeneracy. We further remove 2-fold degenerate events with $\Delta\chi^2 > 10$ where one solution is significantly favoured. This leaves us with 20 planets with exactly two solutions and 12 with more than two solutions.

Among the 20 planets with exactly two solutions [26–45], five are excluded: KMT-2016-BLG-1107 [39] because it is a different type of degeneracy: two distinct source trajectories crossing the $s < 1$ planetary caustic, one of which is parallel to and does not intersect with the binary axis, OGLE-2017-BLG-0373 [26] because it is an accidental degeneracy without complete temporal coverage of the caustic entrance/exit, and KMT-2019-BLG-0371 [44] because of the large mass-ratio ($q \sim 0.1$). As discussed in the next section, the offset degeneracy discussed here only *strictly* manifests when $q \ll 1$. We also exclude OGLE-2016-BLG-1227 [45] and OGLE-2016-BLG-0263 [38] because in both cases $s_{min,max} \sim 4$ makes difficult to include in Fig. 3 scale-wise, and because both cases are deep in the $|1 - s| \gg q^{1/3}$ limit, and are thus already well-characterised by the *inner-outer* degeneracy.

We also inspected events with more than two degenerate solutions, and found that the 4 solutions of KMT-2019-BLG-1339 [46] is comprised of two pairs of degeneracies in alignment with the offset degeneracy, together with the pair of degenerate solutions of MOA-2015-BLG-337 [47] with the smaller mass-ratios.

Beyond the total 17 degenerate events retrieved from the NASA microlensing exoplanet archive and discussed above, we further looked for relevant events in the literature that are not included in the NASA exoplanet archive. Additions include the pairs of solutions with planetary mass-ratios for OGLE-2011-BLG-0526 [48] and OGLE-2011-BLG-0950 [48], as well as the four events with degenerate solutions recently reported in [49]. We also include OGLE-2019-BLG-0960 [20]. This results in a final sample of 25 pairs of solutions in 24 events.

⁵retrieved August 23rd

Range of applicability of the offset degeneracy

Here we provide qualitative considerations of the regimes where the offset degeneracy operates, focusing on the range of q where it manifests as well as on the nature of the degeneracy for caustic-crossing events.

When considering larger mass ratios q , we find the qualitative structure of the *null* persists through $q \rightarrow 1$ (Extended Data Figure 3,4), suggesting that the some form of the *offset* degeneracy may manifest even for $q \gtrsim 0.1$ events. In this regime, there should also be a transition point similar to the *close-wide* degeneracy that results in $x_{\text{null}} = 0$, but $q_A = q_B$ may not hold, nor does $s_A = 1/s_B$. In fact, in the quadrupole and pure-shear approximation, the analogy to the *close-wide* degeneracy requires $\hat{Q} = \gamma$, where $\hat{Q} = s_c^2 \times q_c / (1 + q_c)^2$ is the quadrupole moment of the close central caustic, and $\gamma = (1/s_w)^2 \times q_w / (1 + q_w)$ is the shear of the wide central caustic [8]. Furthermore, it is not clear if the values of $q_{A,B}$ at the $x_{\text{null}} = 0$ *close-wide-equivalent* transition point remains constant when one of s_A and s_B undergoes *offset*. A notable example in the literature is KMT-2019-BLG-0371 [44] where the source trajectory passes through the null created by the two degenerate solutions but $q_A = 0.123$ and $q_B = 0.079$ are significantly different. The exact behaviour of the *offset* degeneracy for $q \rightarrow 1$ should be studied in future work.

We also note that *offset*-degenerate, caustic crossing events usually require vertical trajectories because of the additional constraint on the caustic-crossing length. However, oblique trajectories are allowed if the change in caustic-crossing width near x_{null} is small for both solutions (e.g. OGLE-2019-BLG-0960 [20]).

Relevant prior work

Yee et al. [20] suggested the idea of a “‘close’-‘wide’ degeneracy for semi-resonant caustics” which we summarise below. In the analysis of the planetary event OGLE-2019-BLG-0960, Yee et al. [20] pointed out that the two-fold degeneracy seen in that event is similar to the *close-wide* degeneracy but not fully consistent with it. First, although both solutions are in the resonant regime and do not satisfy the $|\log(s)| \gg 0$ condition⁶ required by the *close-wide* and the *inner-outer* degeneracies, a degeneracy remains. Second, although one solution satisfy $s < 1$ and the other $s > 1$, the $s \leftrightarrow s^{-1}$ correspondence is not exactly satisfied. They further noticed the prevalence of degeneracies for semi-resonant caustics for previously published events, and suggested that in the resonant regime of $\log(s) \rightarrow 0$, the two degeneracies merge.

The *offset* degeneracy provides an alternative picture to [20]: the primary reason that the two degenerate solutions deviated from the $s \leftrightarrow s^{-1}$ correspondence is that $x_{\text{null}} = u_0 / \sin \alpha \neq 0$, and the resonant condition ($\log(s) \rightarrow 0$) only serves to make the asymmetry from $\log(s) = 0$ immediately noticeable. In this specific case, $\log_{10}(s_{\text{close}}) \simeq -0.001$ but $\log_{10}(s_{\text{wide}}) \simeq 0.01$, differing by an order of magnitude. In fact, the same deviation from $s \leftrightarrow s^{-1}$ would persist even if the mass-ratio had been so small ($q \rightarrow 0$) that both solutions were deep in the non-resonant regime ($|1 - s| \gg q^{1/3}$), where the *close-wide* degeneracy is expected to hold exactly.

The theoretical follow up work of [21] sheds additional insight on the current issue. They first clarified that rather than $|\log(s)| \gg 0$, the exact condition of the *close-wide* degeneracy is $|1 - s| \gg q^{1/3}$, which is dependent on the mass ratio. Furthermore, even for $|1 - s| \lesssim q^{1/3}$, the central caustic could still be locally invariant under $s \leftrightarrow s^{-1}$ for parts of the caustic satisfying $|1 - se^{i\phi}| \gg q^{1/3}$, where ϕ is a parametric variable that describes the position along

⁶which [21] clarified to be $|1 - s| \gg q^{1/3}$

the caustic. They concluded by suggesting that slight changes to $s_{A,B}$ and $q_{A,B}$ may create a local pair of degenerate models, which in some sense anticipated our discovery. Furthermore, they suggested that studying caustic resemblances may result in mathematical insight because the magnification pattern is dominated by caustic-crossings and cusp approaches. For caustic-crossing trajectories, the *offset* degeneracy matches the caustic-crossing length of the two degenerate caustics, which is in line with this suggestion to study caustics. However, for non caustic-crossing events, instead of studying caustic properties, it may be more fruitful to directly study the magnification-matching properties at the location of the source.

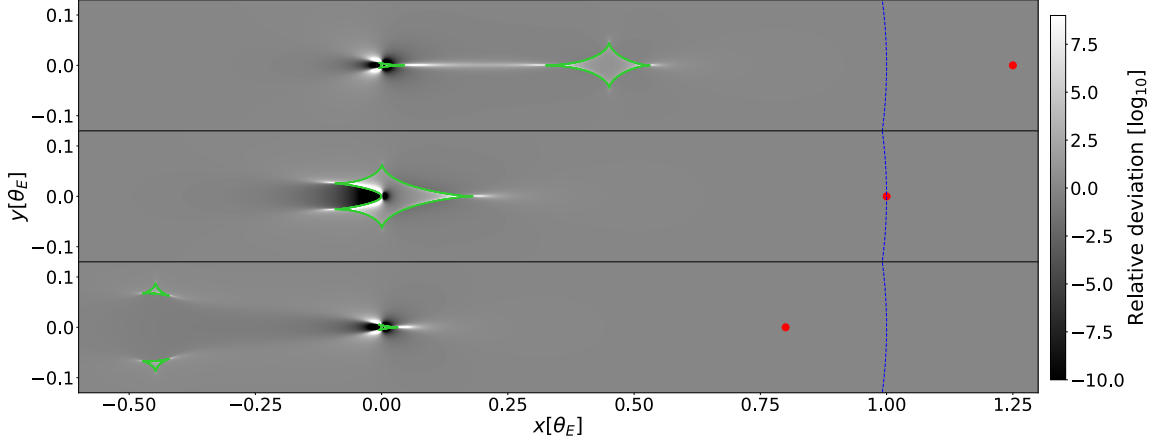
Data Availability Statement

Data on previously published events that support the findings of this study are available in the NASA microlensing exoplanet archive, <https://exoplanetarchive.ipac.caltech.edu>.

References

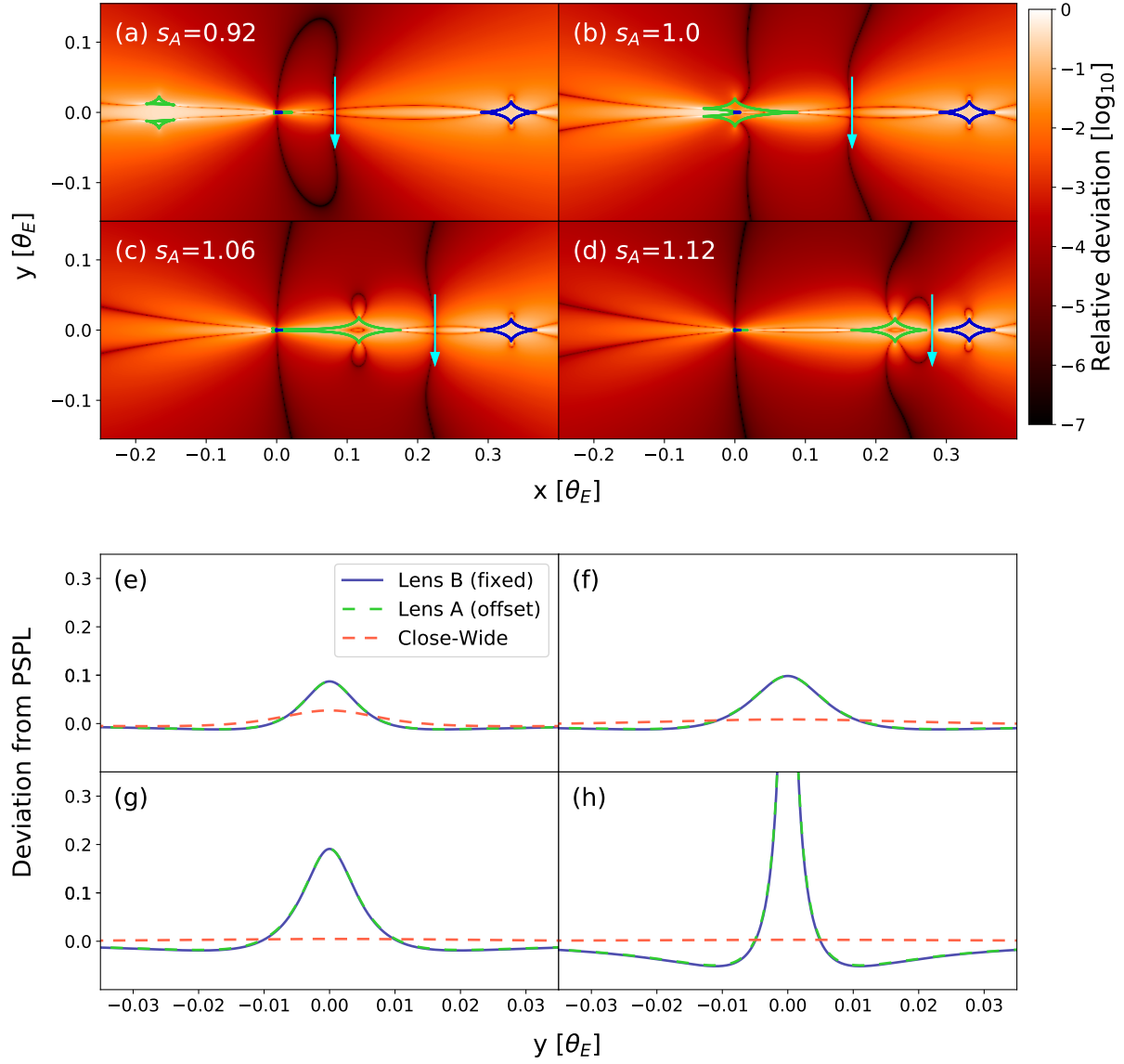
- [23] Yeo, I.-K. A new family of power transformations to improve normality or symmetry. *Biometrika* **87**, 954–959 (2000). URL <https://academic.oup.com/biomet/article-lookup/doi/10.1093/biomet/87.4.954>.
- [24] Gerber, F. & Furrer, R. optimParallel: An R Package Providing a Parallel Version of the L-BFGS-B Optimization Method. *The R Journal* **11**, 352–358 (2019). URL <https://doi.org/10.32614/RJ-2019-030>.
- [25] Byrd, R. H., Lu, P., Nocedal, J. & Zhu, C. A Limited Memory Algorithm for Bound Constrained Optimization. *SIAM Journal on Scientific Computing* **16**, 1190–1208 (1995). URL <http://epubs.siam.org/doi/10.1137/0916069>.
- [26] Skowron, J. *et al.* OGLE-2017-BLG-0373Lb: A Jovian Mass-Ratio Planet Exposes A New Accidental Microlensing Degeneracy. *Acta Astron.* **68**, 43–61 (2018). [1802.10067](#).
- [27] Janczak, J. *et al.* Sub-Saturn Planet MOA-2008-BLG-310Lb: Likely to be in the Galactic Bulge. *ApJ* **711**, 731–743 (2010). [0908.0529](#).
- [28] Hirao, Y. *et al.* OGLE-2012-BLG-0724Lb: A Saturn-mass Planet around an M Dwarf. *ApJ* **824**, 139 (2016). [1604.05463](#).
- [29] Nagakane, M. *et al.* MOA-2012-BLG-505Lb: A Super-Earth-mass Planet That Probably Resides in the Galactic Bulge. *AJ* **154**, 35 (2017). [1703.10769](#).
- [30] Suzuki, D. *et al.* MOA-2008-BLG-379Lb: A Massive Planet from a High Magnification Event with a Faint Source. *ApJ* **780**, 123 (2014). [1311.3424](#).
- [31] Dong, S. *et al.* Microlensing Event MOA-2007-BLG-400: Exhuming the Buried Signature of a Cool, Jovian-Mass Planet. *ApJ* **698**, 1826–1837 (2009). [0809.2997](#).
- [32] Herrera-Martín, A. *et al.* OGLE-2018-BLG-0677Lb: A Super-Earth Near the Galactic Bulge. *AJ* **159**, 256 (2020). [2003.02983](#).

- [33] Rattenbury, N. J. *et al.* Faint-source-star planetary microlensing: the discovery of the cold gas-giant planet OGLE-2014-BLG-0676Lb. *MNRAS* **466**, 2710–2717 (2017). [1612.03511](#).
- [34] Bond, I. A. *et al.* The lowest mass ratio planetary microlens: OGLE 2016-BLG-1195Lb. *MNRAS* **469**, 2434–2440 (2017). [1703.08639](#).
- [35] Han, C. *et al.* MOA-2016-BLG-319Lb: Microlensing Planet Subject to Rare Minor-image Perturbation Degeneracy in Determining Planet Parameters. *AJ* **156**, 226 (2018). [1809.07898](#).
- [36] Bennett, D. P. *et al.* MOA Data Reveal a New Mass, Distance, and Relative Proper Motion for Planetary System OGLE-2015-BLG-0954L. *AJ* **154**, 68 (2017). [1705.03937](#).
- [37] Hirao, Y. *et al.* OGLE-2013-BLG-1761Lb: A Massive Planet around an M/K Dwarf. *AJ* **154**, 1 (2017). [1703.07623](#).
- [38] Han, C. *et al.* OGLE-2016-BLG-0263Lb: Microlensing Detection of a Very Low-mass Binary Companion through a Repeating Event Channel. *AJ* **154**, 133 (2017). [1708.02727](#).
- [39] Hwang, K.-H. *et al.* KMT-2016-BLG-1107: A New Hollywood-planet Close/Wide Degeneracy. *AJ* **157**, 23 (2019). [1805.08888](#).
- [40] Han, C. *et al.* Four microlensing planets with faint-source stars identified in the 2016 and 2017 season data. *A&A* **642**, A110 (2020). [2008.09258](#).
- [41] Ranc, C. *et al.* OGLE-2015-BLG-1670Lb: A Cold Neptune beyond the Snow Line in the Provisional WFIRST Microlensing Survey Field. *AJ* **157**, 232 (2019). [1810.00014](#).
- [42] Nucita, A. A. *et al.* Discovery of a bright microlensing event with planetary features towards the Taurus region: a super-Earth planet. *MNRAS* **476**, 2962–2967 (2018). [1802.06659](#).
- [43] Han, C. *et al.* Three microlensing planets with no caustic-crossing features. *A&A* **650**, A89 (2021). [2104.06544](#).
- [44] Kim, Y. H. *et al.* KMT-2019-BLG-0371 and the Limits of Bayesian Analysis. *AJ* **162**, 17 (2021). [2101.12206](#).
- [45] Han, C. *et al.* OGLE-2016-BLG-1227l: A wide-separation planet from a very short-timescale microlensing event. *The Astronomical Journal* **159**, 91 (2020). URL <https://doi.org/10.3847/1538-3881/ab6a9f>.
- [46] Han, C. *et al.* KMT-2019-BLG-1339L: An M Dwarf with a Giant Planet or a Companion near the Planet/Brown Dwarf Boundary. *AJ* **160**, 64 (2020). [2003.02375](#).
- [47] Miyazaki, S. *et al.* MOA-2015-BLG-337: A Planetary System with a Low-mass Brown Dwarf/Planetary Boundary Host, or a Brown Dwarf Binary. *AJ* **156**, 136 (2018). [1804.00830](#).

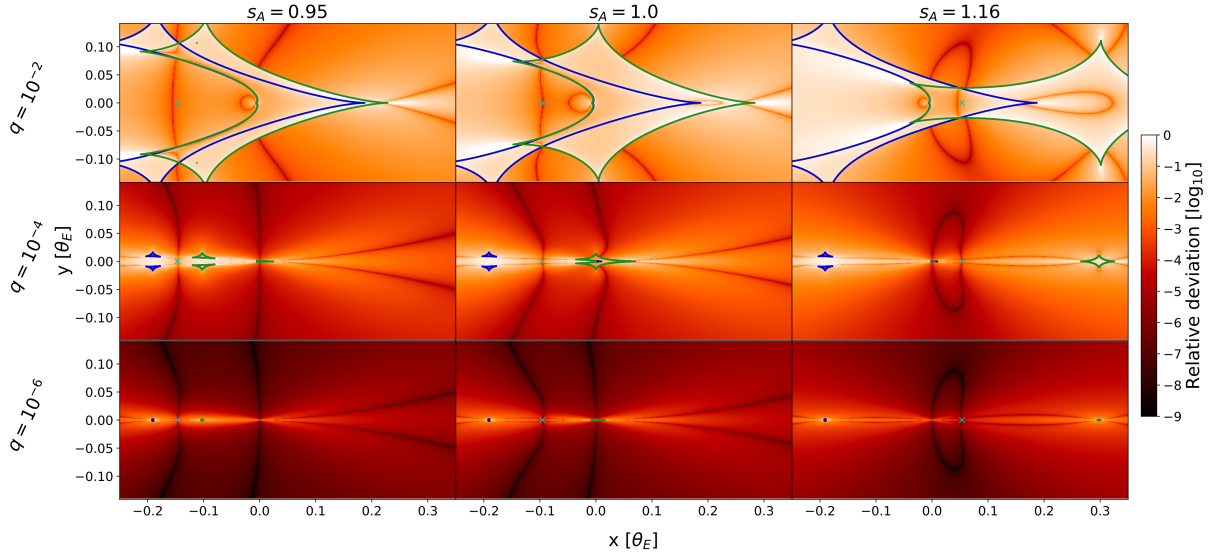


Extended Data Figure 1: Caustics shown in green atop of maps of magnification differences from a 1-body lens, for wide (top), resonant (middle), and close (bottom) caustic topologies. Red dots indicate locations of the planet, with separations $s = 1/0.8, 1, 0.8$ from the host star, located at the origin. Blue dashed lines represent the Einstein ring θ_E , the angular size of to which the projected separation (s) is normalised. Caustic topologies are delineated by values of s for a given q . In the wide regime ($s \gtrsim 1 + (3/2)q^{1/3}$), there is one central caustic located near the host star and one asteroid-shaped “planetary” caustic towards the location of the planet. In the close regime ($s \lesssim 1 - (3/4)q^{1/3}$), there are two small, triangular shaped “planetary” caustics in addition to the central caustic that appears similar to the wide central caustic, due to the *close-wide* degeneracy. For values of s in between these regimes, there is one six-cusped “resonant” caustic. For all cases, there are lobes of excess magnification compared to a point lens near caustic cusps, and lobes of de-magnification towards the back-end of the central/resonant caustic.

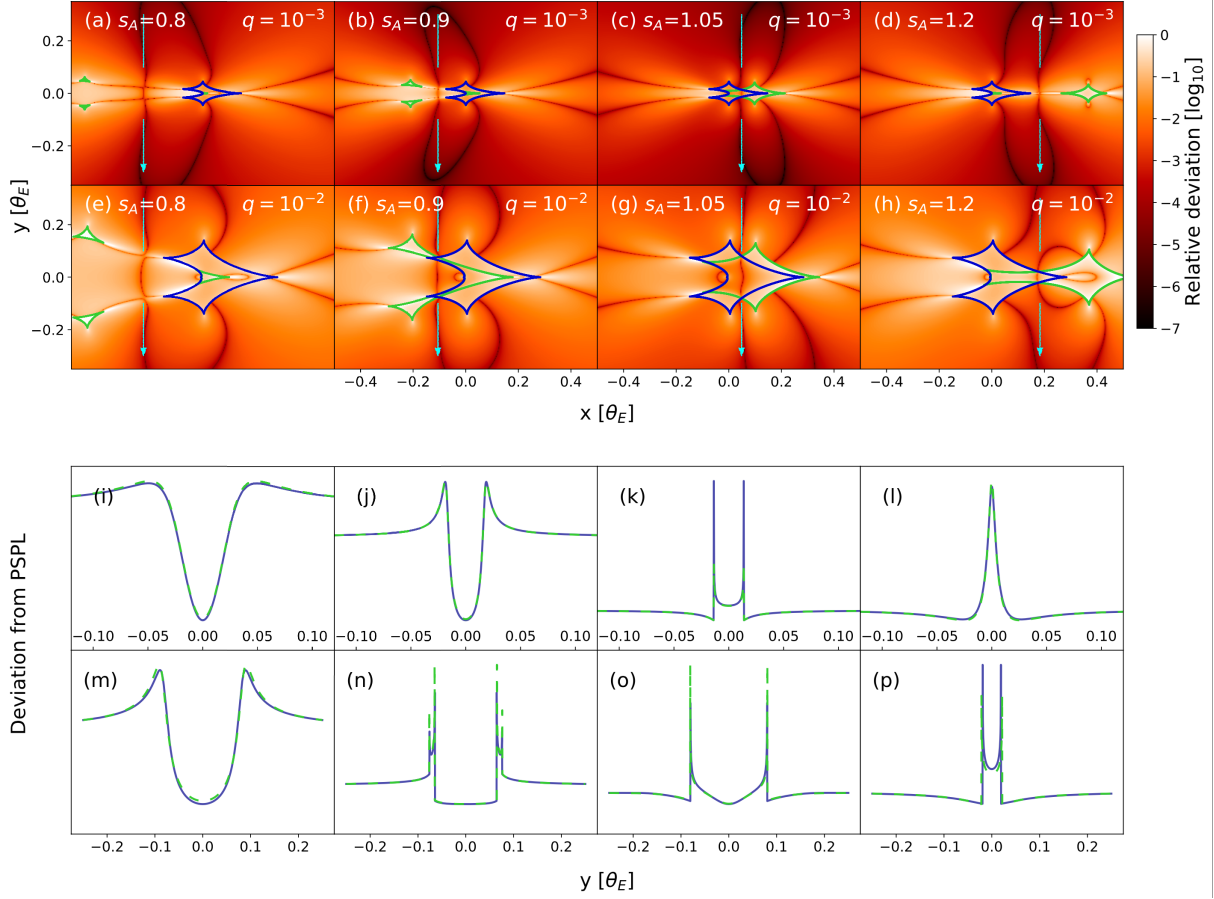
- [48] Choi, J.-Y. *et al.* A New Type of Ambiguity in the Planet and Binary Interpretations of Central Perturbations of High-Magnification Gravitational Microlensing Events. *The Astrophysical Journal* **756**, 48 (2012). URL <https://iopscience.iop.org/article/10.1088/0004-637X/756/1/48>.
- [49] Hwang, K.-H. *et al.* Systematic KMTNet Planetary Anomaly Search, Paper II: Five New $q < 2 \times 10^{-4}$ Mass-ratio Planets. *arXiv:2106.06686* [astro-ph] (2021). URL <http://arxiv.org/abs/2106.06686>. ArXiv: 2106.06686.



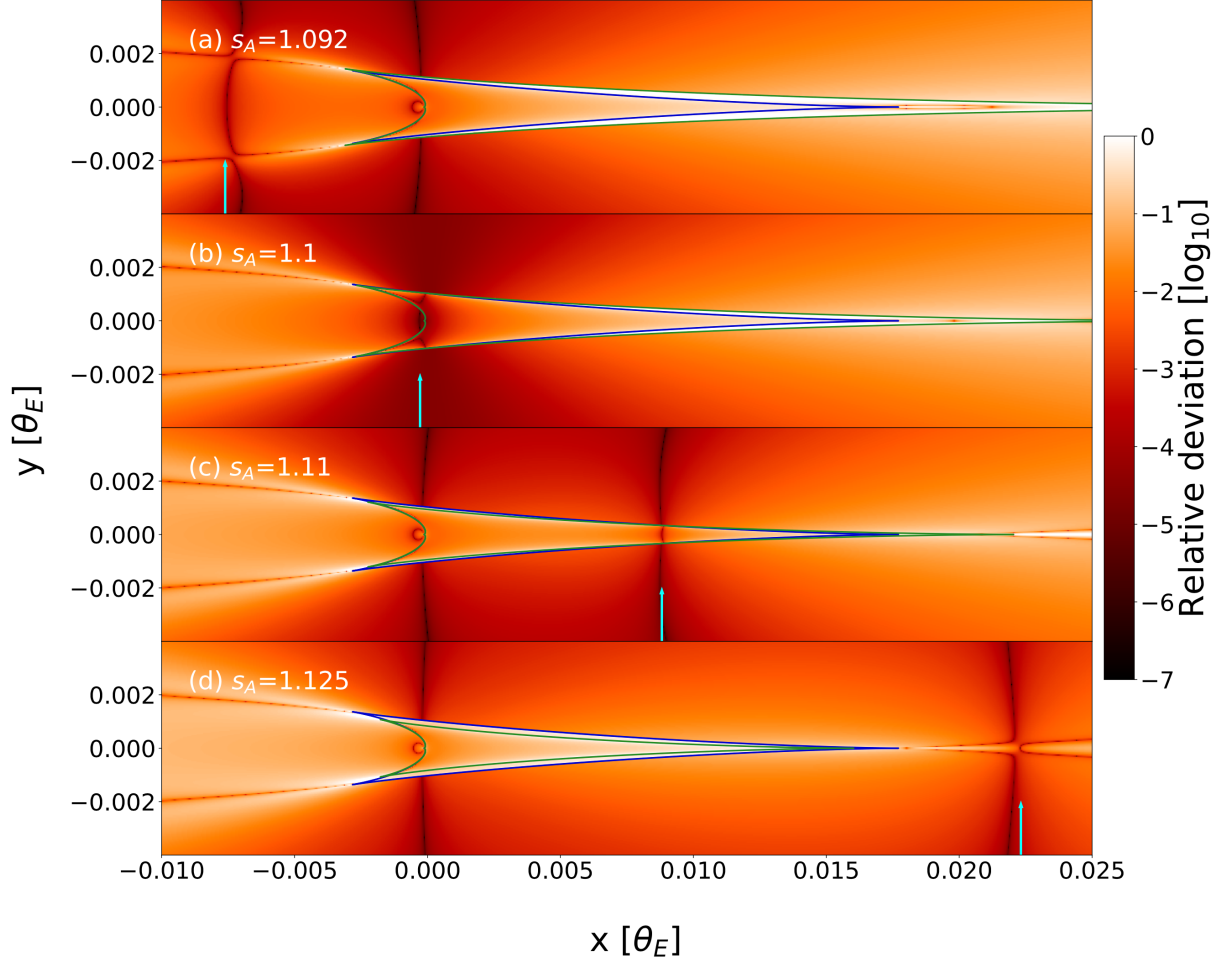
Extended Data Figure 2: Similar to Figure 1, but for fixed $s_B = 1.18 > 1$. This completes the *resonant-close* (b) and wide-topology *inner-outer* (d) cases.



Extended Data Figure 3: Magnification difference maps which demonstrates the *offset* degeneracy independence on q . Lens B shares the same fixed $s_B = 1.1$ as in Figure 1. Each row shows cases of $s_A = 0.95, 1, 1.16$ for $q = 10^{-2}, 10^{-4}, 10^{-6}$. The null location predicted from Equation 1 is shown in cyan crosses. For $q = 10^{-4}$ and $q = 10^{-6}$, the null shape largely remains constant where the null intersection on the star-planet axis is well predicted by the analytic prescription (Equation 1; cyan crosses). The three cases of $q = 10^{-2}$ demonstrate how the behaviour of the null changes as $q \rightarrow 1$. In the case of $s_A = 1.16$, the null is split into two disconnected segments inside and outside of the caustic, where the analytic prediction is close to their mean location. For $s_A = 0.95$, the discrepancy from the analytic prediction may be attributed to the curvature of the null near the star-planet axis.



Extended Data Figure 4: Magnification difference maps similar to Figure 1, but for fixed $s_B = 1$. (i)–(p) shows logarithmic deviations from PSPL on arbitrary scales, where green dashed curves are the changing lens A and solid blue curves are for fixed lens B. (a)–(d) and (e)–(h) show the same sequence of s_A but for $q = 10^{-3}$ and $q = 10^{-2}$ to illustrate how the *offset* degeneracy generalises to larger mass-ratios. (a,e) reveals that the ring structure of the null is composed of two distinct null segments, where one appears to originate from the centre of the central/resonant caustic and the other from the left two cusps of the same caustic. Closer inspection shows that the null rings for (a) and (e) have different topologies: for (a) it is the left part of the null that intersects on the star-planet axis but for (e) it is the right part. This disjoint topology of the null is also seen in Figure 1 and Extended Data Figure 3 & 5. The topology transition point, presumably a function of s and q , may have mathematical implications for the *offset* degeneracy. Furthermore, we observe that the null segment near the star-planet axis becomes increasingly curved for $|\log(s)| \gg 0$ and $q \rightarrow 1$, which may explain how Equation 1 and the *offset* degeneracy in general, may break down in those limits.



Extended Data Figure 5: Magnification difference maps zoomed-in on the central caustic. Same $s_B = 1/1.1$ as Figure 1.